







Thomas Whittaker , Shiyu Zhang , Alexander Powell ,
Chris J. Stevens , John (Yiannis) C. Vardaxoglou ,
and William Whittow 

3D Printing Materials and Techniques for Antennas and Metamaterials

A survey of the latest advances.

This is a review article of the latest advances in 3D printing for enabling new materials and new geometries for radio-frequency (RF) devices, antennas, and metamaterials. The article discusses the achievable material properties and various optimized applications that are achievable by creating new shapes in either dielectric or metal. This article demonstrates what is currently possible with additive manufacturing

and the current limitations. Various additively manufactured RF devices are reviewed.

INTRODUCTION

This article is a review of the latest advances concerning 3D printing for RF, antennas, and metamaterials applications. For many years, RF engineers have been improving performance largely via changing the 2D shape of the metallization enabled, in part, by the recent advances in optimization via simulations. Electromagnetic (EM) performance and manufacturability

Digital Object Identifier 10.1109/MAP.2022.3229298
Date of current version: 23 December 2022

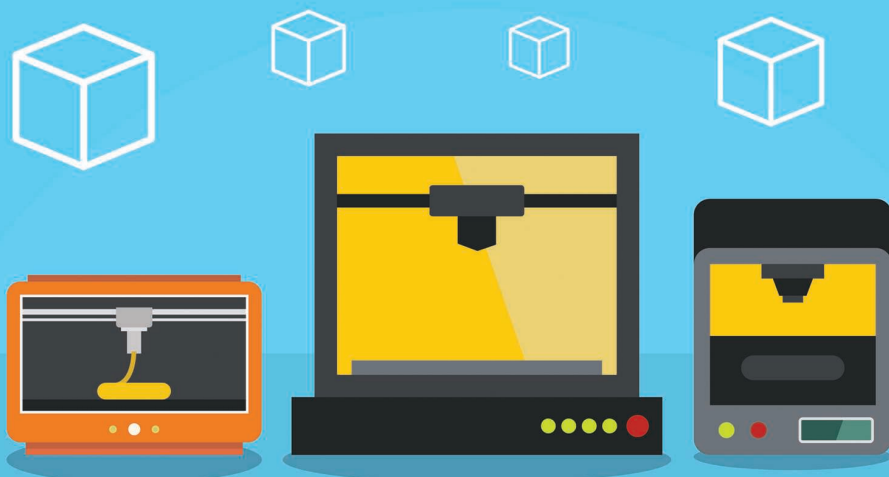


IMAGE LICENSED BY INGRAM PUBLISHING



have always been the major concerns when proposing novel RF designs. In recent years, numerous researchers have demonstrated the EM advantages of 3D engineered EM materials and structures. However, many proposed ideas were not attractive in practice, due to the challenges in manufacturing. In recent decades, antennas and metamaterials fabrication have been dominated by mature subtractive manufacturing methods, such as etching and machining. They are specialized in creating 2D and exterior shapes, but the ability of engineering the internal structures is limited. Thanks to the additive manufacturing process, 3D printing has several advantages that include the ability to fabricate complex internal structures that enable bespoke dielectric properties; the ability to vary and grade the relative permittivity in two and even three axes; the ability to create cheaper, more efficient, and lightweight devices; and the ability to fabricate in 3D. Challenges include the resolution and surface roughness that becomes apparent at higher frequencies, the repeatability from laboratory to laboratory, the capability to 3D print dielectrics and low-loss conductors in the same process step, and the manufacturing challenges of scaling to large volumes. The growth in this area is demonstrated by there being 23 IEEE journal papers related to 3D-printed antennas in the five years between 2012 and 2016 and 211 IEEE journal papers between 2017 and 2021. This article reviews the state of the art in this area. The “Materials and Dielectric Properties” section discusses the achievable material properties and the additive manufacturing processes. The “Comparison of 3D Printing Techniques for RF Applications” section provides a comparison of the different 3D printing methods suitable for different RF applications. The “RF Components Printed With Plastics” section addresses new applications for new 3D-printed dielectric geometries that includes lenses, reflectarrays (RAs), polarizers, and impedance matching devices. The “3D-Printed Ceramic Components” section looks at additively manufactured ceramic components that exhibit low conductive and dielectric losses. The “Metalized Waveguides and Horn Antennas” and “Metaparticles for Isotropic Multimode Microwave Scattering” sections consider metallizing 3D-printed shapes to either enable new complex structures, such as scatterers, or minimize the cost and weight of devices.

MATERIALS AND DIELECTRIC PROPERTIES

FUSED FILAMENT FABRICATION

The most common materials used in fused filament fabrication (FFF) are acrylonitrile butadiene styrene (ABS) and polylactic acid (PLA). These are easy to print using basic off-the-shelf printers. The filaments are designed for their physical properties rather than their EM properties. ABS has a relative permittivity, ϵ_r , of ~ 2.69 and a loss tangent, $\tan \delta$, of ~ 0.012 , while PLA has an ϵ_r of ~ 2.7 and a $\tan \delta$ of ~ 0.008 measured at 1 MHz [1]. The dielectric properties were measured with a range of techniques over the frequency range of 2–60 GHz: ABS had an ϵ_r of ~ 2.45 and a $\tan \delta$ of ~ 0.005 , and PLA had an ϵ_r of ~ 2.55 and

a $\tan \delta$ of ~ 0.009 [2]. There are also lower-loss thermoplastics available with similar ϵ_r properties, such as high-impact polystyrene (HIPS), with an ϵ_r of ~ 2.49 and a $\tan \delta$ of $\sim 8.53 \times 10^{-4}$; polypropylene (PP), with an ϵ_r of ~ 2.03 and a $\tan \delta$ of $\sim 1.45 \times 10^{-4}$; and cyclo olefin copolymer (COC), with an ϵ_r of ~ 2.24 and a $\tan \delta$ of $\sim 2.17 \times 10^{-4}$, which makes these materials attractive for RF applications. The dielectric properties of a range of different 3D-printable materials as a function of processing temperature and the ϵ_r versus the $\tan \delta$ can be found in [3].

As a general rule with 3D-printed dielectrics, it is important to measure the dielectric properties of test printed samples before fabricating a more complex design, as changes to the printer and its settings can affect the ϵ_r and $\tan \delta$ [4]. It is impossible to achieve a 100% dense part, as air voids always exist between the extruded layers of filament. Changing the printer/printing parameters, such as the nozzle width, extrusion speed, material overlap, layer height and temperatures of the nozzle and testbed, can affect the number of air pockets introduced into the final print, which inevitably affects the realized ϵ_r and $\tan \delta$ values. It is recommended to print a range of samples while varying the printing parameters and measure their physical density and dielectric properties to find the optimum settings for your machine to achieve maximally dense parts and the highest effective permittivity. Structural and EM anisotropy is another aspect that may need to be considered due to the nonisotropic way the filament is extruded. Typically, filament is extruded in parallel lines with alternating layers between a 0 and 90° rotation, which tends to lead to different properties for the axes parallel and perpendicular to the print direction. Depending upon the application, this may need to be factored into the design.

3D-printable filaments are now being developed for their dielectric properties. These are typically manufactured by mixing high-permittivity ceramic additives, such as barium titanate powder, with thermoplastics and extruding them into filaments [5], [6]. They can exhibit an increased ϵ_r but often have higher losses and are more challenging to print. With a higher ceramic content, the filament becomes more brittle, and there is an increased likelihood of nozzle blockages occurring. A ceramic infill is required in a nanoparticulate form for the high ceramic loading to improve the printability and prevent extrusion blockage. Similarly, commercial filaments are available from PREPERM, with an ϵ_r of $\sim 2.9, 4.4, 5.8, 7.6, 9.6, 11.9$ and a $\tan \delta$ of ~ 0.004 at ~ 2 GHz. Optimizing the printer's settings for maximally dense parts is especially important for these ceramic-loaded filaments since any introduced air pockets will have a greater impact upon the realized ϵ_r value of the print [4]. The challenges to achieve a good quality print, especially for complicated geometries, increase as the ϵ_r increases, as the filaments are designed for their ϵ_r [4]. The dielectric properties and loss tangent values of a range of thermoplastics are plotted in Figure 1.

VAT POLYMERIZATION

The vat polymerization methods of additive manufacturing involve a light source selectively curing photocurable resin in a tank. Since the parts are effectively drawn with light, parts with fine details are possible, though the photocurable resins used often have high loss tangent values. Resin-based photocurable polymer materials for stereolithography were characterized over the frequency range of 0.2–1.4 THz by using time domain spectroscopy; the ϵ_r was ~ 2.8 , and the $\tan \delta$ was ~ 0.08 [7]. Ceramic-loaded resins are available with higher permittivity and lower loss tangent values achievable; the part can also be fired afterward to burn off the resin and sinter the remaining ceramic powder [8]. Extra consideration of internal voids is needed for vat polymerization since drain holes need to be placed to clear them. Multimaterial prints are difficult to achieve with vat polymerization since multiple vats and intermediate washing stations are required, which increases greatly the complexity and cost of the process. The dielectric properties and loss tangent values of clear and ceramic-loaded resin (after firing) are plotted in Figure 1.

POWDER BED FUSION

The powder bed fusion (PBF) processes involve incrementally filling a tank with a polymer/ceramic/metal powder and using a heat source (typically a laser) to melt the top powder layer to form the part. Once finished, the part is suspended in the unmelted powder in the tank. These machines are several orders of magnitude more expensive than desktop dielectric 3D printers and are also expensive to run and maintain. Porosity

and surface roughness are potential issues of PBF methods, and an understanding of your printing parameters and material is required to minimize these issues [9], [10]. Sand/bead blasting and tumbling are potential postprocessing options available, which could also be used to polish surfaces of these prints and reduce losses. One great advantage with this method is that parts can be printed directly in ceramic and metal, which allows the use of higher-permittivity/lower-loss dielectrics (compared to polymers) and conductors with lower resistivity (compared to conductive inks).

3D PRINTING WITH CERAMICS SLURRIES

Using specialist material processing techniques, it is possible to process and 3D print high-permittivity, low-loss ceramics. One such process is direct ink writing (DIW), which involves extruding viscous ceramic slurries in a similar manner to FFF. The extruded part (known as a *green body*) then undergoes a drying process before it is sintered. With DIW, it has been shown that processing materials with an ϵ_r of ~ 35 and a $\tan \delta$ of < 0.0001 can be achieved [11]. This process can also print with metal slurries alongside ceramics [12], [13], though the thermal expansion coefficients of the two materials need to be matched; otherwise, the green body will warp or crack during sintering. Out of the processes mentioned in this review, ceramics printed with DIW generally deliver the lowest-loss, highest-permittivity materials, with the capability of processing metals close to their bulk conductivity value in the same printed part. The dielectric properties and loss tangent values of a range of low- and high-sintering-temperature ceramics are included in Figure 1.

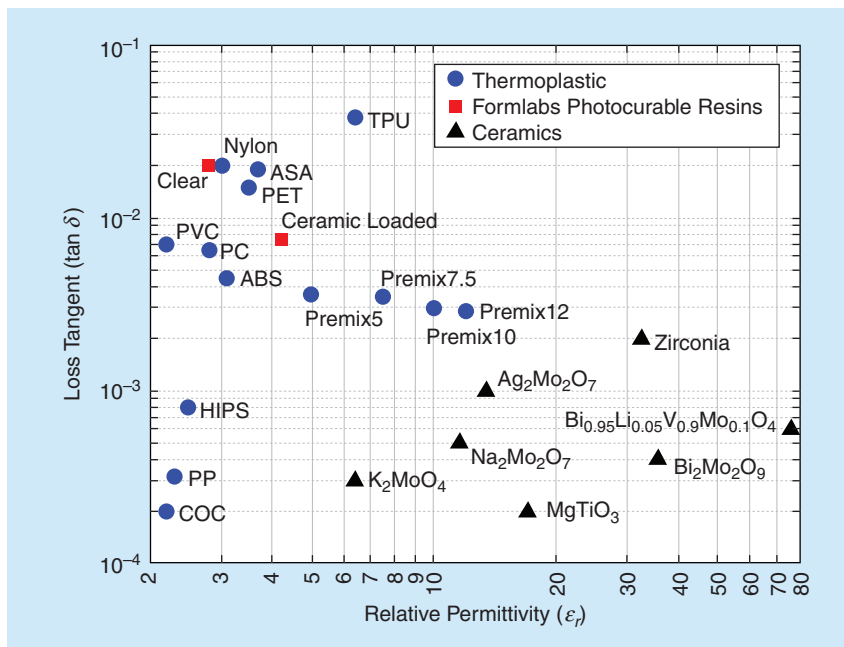


FIGURE 1. The dielectric constant and loss tangent values of various thermoplastics, resins, and ceramic dielectric materials: acrylic styrene acrylonitrile (ASA), ABS, COC, HIPS, polycarbonate (PC), polyethylene terephthalate (PET), polyvinyl chloride (PVC), PP, and thermoplastic polyurethane (TPU). The data were collected from academic literature and split-post dielectric resonator measurements at Loughborough University.

3D PRINTING WITH CONDUCTIVE MATERIALS

Achieving metalized parts can be tricky. Often, the part is printed in a dielectric material first, and metallization is achieved afterward by coating the required regions with a conductive ink/paint [14], [15] or by manually adding copper tape. Large areas of copper tape are easy to add and have good conductivity, while conductive inks/paints tend to have conductivity values lower than that of bulk metals but can be applied to complicated geometries. Since the 3D-printed parts are only for supporting the outer conductive surface, the core structure can be printed using high-resolution printing techniques, such as stereolithography and selective laser sintering (SLS)/melting, to achieve high geometry accuracy and good surface roughness. Surface polishing processes can be applied to the printed parts, such as sand/bead blasting and tumbling,

to further improve the surface roughness that is particularly important for high-frequency applications. These methods are great for research and proving concepts but not necessarily suitable for repeatable and robust mass manufacturing.

An alternative to metalizing the 3D dielectric is to print the structure directly in a metal, which removes one processing step. A conducting commercial FFF-compatible filament, Electrifi, is available, which can be printed as with conventional filaments. The stated conductivity is $\sigma \sim 1.67 \times 10^4$ S/m [1]; however, achieving this value can be challenging in practice. This relatively low conductivity is likely to lead to high losses in antennas; however, the filament could be effective as a shielding material. Electrifi has been used to 3D print RFID tags; ridges in the substrate were introduced to enable some miniaturization, but the read range was reduced from 8 m, with a copper tag, to 2 m, with Electrifi [16]. Electroplating the surface can improve the conductivity by >100 times [17].

An innovative method to create embedded 3D conducting structures was to introduce air channels with an inlet and an exit hole [3] in the 3D-printed structure. These channels were then filled afterward with Field's metal, which has a melting temperature of 65 °C. This method is often compatible with FFF-printed thermoplastic parts, which often have glass transition temperatures at ~100 °C. By using a fine 0.2-mm nozzle, repeatable printing of 0.4-mm channels could be achieved that did not leak. 3D resonant metamaterials were designed in this way [3].

PBF techniques allow the direct printing of metal components; however, surface roughness is a potential issue, which can increase loss. This technique was used to create waveguides and power dividers [18], a lightweight and cost-effective panel antenna in the millimeter waveband [19], a 3D beam scanning leaky wave antenna array at 30 GHz [20], and a wideband circularly polarized (CP) waveguide array antenna consisting of four antipodally ridged elements and a compact feeding network [21]. The example in [19] showed a comparison between a computer numerical control (CNC)-machined antenna and a SLS-printed antenna; on average, the SLS-printed antenna was 11% and 13% less efficient in the K- and Ka-bands, respectively, largely owing to increased surface roughness. The reader should note that accumulated losses associated with physical joints in conventionally manufactured parts (e.g., waveguide flange joints) could be greater than the surface roughness losses of 3D-printed parts since these parts can be printed in one go without the need for

joints. The example also found that the CNC-machined antenna had consistently lower dimensional errors compared to the design than the SLS-printed antenna. These factors illustrate that 3D printing is not a direct replacement for conventional manufacturing techniques, and often, the desired part needs to be optimized for the 3D printing method. As shown in [22], where different 3D printing methods were used to fabricate 3D Hilbert fractal antennas, each method has a tradeoff among cost, weight, physical robustness, and EM performance.

ARTIFICIAL DIELECTRICS

It is well known that if two dielectric materials are mixed, then the mixture forms an artificial dielectric, where the effective properties are likely to be between the two properties of the constituent materials. This holds true as long as the inclusion is much smaller than a wavelength ($l < \lambda/10$) [23]. Subresonant metallic inclusions can also be mixed with a dielectric host material, which will increase the effective permittivity but also reduce the effective permeability. Manufacturing artificial dielectrics is time-consuming to do via conventional manufacturing, but 3D printing naturally lends itself to creating these internal geometries, and the software typically requests a “volume infill percentage” setting for the print. Artificial dielectrics are a simple way of varying the EM material properties across the structure by using only one or two constituent materials [24]. An example of this is a flat graded-index (GRIN) lens, where the dielectric constant was varied across its volume [25]. The choice of infill pattern will also influence the EM performance and may lead to an anisotropic ϵ_r in two axes.

COMPARISON OF 3D PRINTING TECHNIQUES FOR RF APPLICATIONS

Table 1 summarizes the pros and cons of selective 3D printing techniques that have been applied for RF applications. The maximum print volume used to be one of the key factors in choosing the printing technique, but this was negated with the development of new bespoke machines with large build volumes. In addition, large geometries can also be split into multiple small parts to be printed separately [26]. Some of the polymer-based materials can benefit from using compatible solvents to join the bonding surfaces together without leaving extra materials after evaporation and curing. For instance, acetone (propanone) can be used for dissolving ABS material, and

TABLE 1. THE COMPARISON OF DIFFERENT ADDITIVE MANUFACTURING METHODS.

Technique	Resolution (Low, Medium, and High)	Option of Customized Materials	Multimaterial Printing	Metal Printing	Postprocessing
FFF	L to M	Many	Yes	Yes	No
Vat polymerization (e.g., digital light processing, stereolithography, and so on)	Medium to high	Few	No	No	Yes
PBF (SLS and selective laser melting)	Medium to high	Almost none	No	Yes	Yes
DIW	Low to medium	Few	Yes	Yes	Yes
Material jetting (e.g., PolyJet)	Medium to high	Almost none	Yes	No	Yes

D-limonene can be used for HIPS. Figure 2 shows a 3D-printed dielectric transmitarray (TA) that is composed of five parts. The TA was printed using ABS-based materials, and acetone was used for bonding. The bonding surface does not affect the TA performance but provides good mechanical strength.

FFF and DIW allow multimaterial printing using customized RF-graded materials. This is the major advantage of these two techniques even though they do not provide the high resolution of their counterparts. Although FFF and DIW cannot directly print metal as the PBF, they support printing conductive materials, which are equivalent to metal in RF applications. The conductive materials are usually made into paste so that they can be extruded using a nozzle. The extrusion process can be easily integrated into the multimaterial FFF processes. Figure 3(a) demonstrates the process of printing a metacapacitor by using a hybrid FFF printing method [28]. The conductive meta-atoms are printed using silver-based paste and can be fully sealed inside the thermoplastic material. The entire printing process is finished in a single step. Most conductive pastes require curing

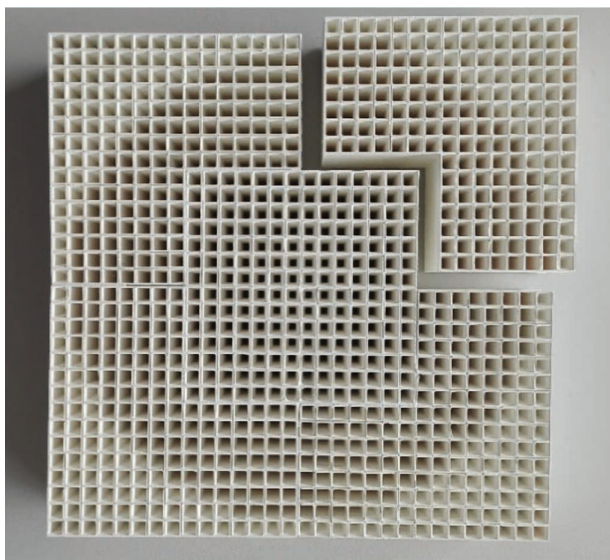


FIGURE 2. A 3D-printed perforated dielectric transmitarray (TA) with total dimensions of $180 \times 180 \times 32$ mm. The entire TA was printed in five parts using PREPERM ABS4.4 and then bonded using acetone. For more information, see [27].

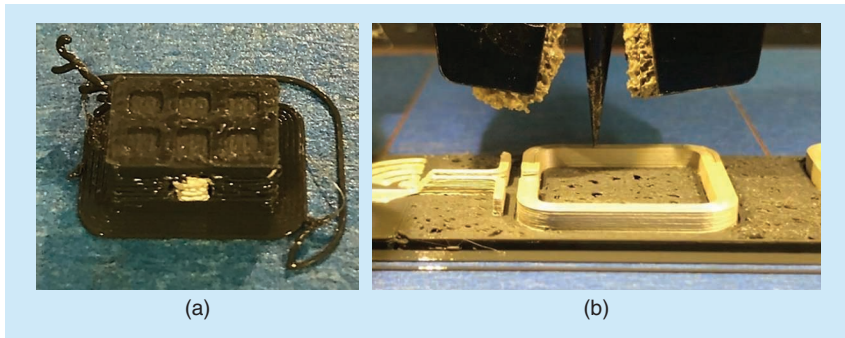


FIGURE 3. Melted thermoplastics and an air-curable silver ink. (a) A 3D metacapacitor before the meta-atoms are printed. (b) Superdirective dimers of coupled self-resonant split-ring resonators. For more information, see [28] and [29].

to achieve their highest conductivity. In recent years, fast-curing and curing-free conductive pastes have become available. The viscosity of the conductive paste can be increased, so the paste layers can be stacked up with a good vertical wall definition. Figure 3(b) illustrates the printing of superdirective dimers of coupled self-resonant split-ring resonators. The increased height of the split-ring resonators was printed using a curing-free silver-based paste to allow stand-alone tall conductive walls.

Despite not supporting multimaterial printing, vat polymerization and PBF usually offer high-resolution printing, so the surface roughness is visibility finer compared with the FFF-printed surface [shown in Figure 4(a)]. This makes them more popular in high-millimeter-wave and subterahertz applications when compared with FFF. Another advantage of vat polymerization and PBF is being able to print complex overhanging structures. The unfused powder and uncured liquid of the support structures and can be easily removed in postprocessing. Figure 4(b) details an interlaced metamaterial mesh structure that was printed using SLS.

RF COMPONENTS PRINTED WITH PLASTICS

3D-PRINTED LENSES

Dielectric lenses are well-known techniques to alter wavefronts and increase gain. The simplest dielectric lenses are hemispherical in shape and made from homogeneous dielectrics. 3D-printed examples at different frequencies include samples at 10.7 [31], 60 [32], and 120 GHz [33]. At these high frequencies, care needs to be taken, and accurate machines need to be used, or the finished product may have limited accuracy. It was found that a fabrication error of ± 0.127 mm in the lens design led to a phase error of 1.63° at 13.4 GHz [34]. Clearly, these errors will become more significant at higher frequencies. The same paper discusses how the use of geometrical optics can alter the focal point to adjust for misprinted lenses [34].

The same performance can be achieved by varying the local relative permittivity instead of the shape; these are called *GRIN lenses*, as presented in Figure 5. The GRIN lens is composed of a series of concentric rings, where the highest relative permittivity is at the center and the lowest value is at the outer ring [25]. The thickness of the lens is defined by the focal length and

maximum relative permittivity of the material. Ideally, the lens should have a smooth variation in the effective permittivity, analogous to the curvature of the hemispherical homogeneous lens. In practice, this is difficult to print, and it has been found that having six rings of varying permittivity is sufficient to emulate a smooth variation and achieve a similar gain to the smooth transition. The design is frequency independent but in practice is limited by the resolution of the printer since air voids that are introduced into the outer rings to lower the effective permittivity will have

an inherent resonant frequency. The thickness of the lens can be reduced by starting with a higher relative permittivity of the host material and adding subresonant metallic inclusions to increase the effective permittivity of the artificial dielectric [25]. The losses of the dielectric material do not have a significant impact on the achieved gain of the lens. It is worth noting that using ϵ_r materials may affect the effectiveness of the lens, due to increased reflections as waves transition from air to the lens. A quarter-wavelength matching layer could be used here to improve the impedance mismatch, though this implementation would be frequency limited. GRIN lenses have been placed inside horn antennas to increase the gain [35]. Similarly, the gain of a horn antenna was increased by designing a higher ϵ_r in the middle and an ϵ_r close to air (by minimizing the volume fraction of the 3D-printed filament) at the edges of the circular horn antenna [36]. Integrating lenses into the antenna structure is an attractive use since the required focal length normally increases the size of the antenna system. In a related area, horn antennas have been filled with 3D-printed materials for biomedical applications. The aim was not to increase the gain but to match the impedance of the antenna to the human body to minimize reflections at the interface between air and body [37], [38], [39].

Another common alternative lens configuration is the Fresnel lens, where grooved concentric rings shape the wavefront of the illuminating beam; these lens designs are thinner and lighter than hemispherical lenses. 3D printing also provides the option of varying the local shape and local effective permittivity to make a hybrid lens, which further increases the gain of the lens [40]. By printing a block with two different relative permittivity values, where the ϵ_r varies locally, it is possible to engineer lenses with advanced capability. For example, a bifocal lens was designed, 3D printed, and measured, where the incident wave was directed in two different directions at two different frequencies [41]. The complex internal geometry was composed of two different dielectric materials that were topologically optimized, which could not have been achieved using conventional manufacturing techniques.

Conventionally, we use lenses to increase the gain of the antenna system. However, it is possible to design lenses that increase the beamwidth and hence reduce the maximum gain. An example of this used a 3D-printed lens to increase the 3-dB axial ratio beamwidth from 82° to 162° of a CP antenna [42]. This lens functioned over a wide bandwidth. Using a lens to increase the gain of the antenna is attractive, but often, the system

architecture requires the ability to steer the beam. This is achieved by changing the feeding position relative to the lens. The most common examples of lenses used to achieve beam steering are Luneburg lenses (LLs) [43], [44], [45], [46]. 3D printing allows the lens to be tailor-made by using dual materials and varied local ϵ_r increases. A spherical LL was converted into an ellipsoidal shape via transformation optics to increase the lens' aperture efficiency [44]. By carefully designing the shape and varying the local ϵ_r by using the 3D printing degrees of freedom, it was possible to minimize the size requirements and number of feeds required [44].

POLARIZATION CONVERTERS

Efficient polarizers can be produced by 3D printing anisotropic structures; for example, a dielectric slab with rectangular slots of air orientated at 45° to the electric fields can convert a linearly polarized beam into a CP beam [48]. The performance is wideband, and the limiting factor is when the width of the slots/dielectric strips approaches a wavelength. 3D printing also facilitates the combination of polarizer functionality with a lens design to create a single device [49], [50]. In [50], the functionality of Wollaston and Rochon prisms was integrated into 3D-printed lenses to generate and separate left- and right-handed CP beams at 30 GHz. The required phase change was introduced by changing the physical geometry of the unit cells.

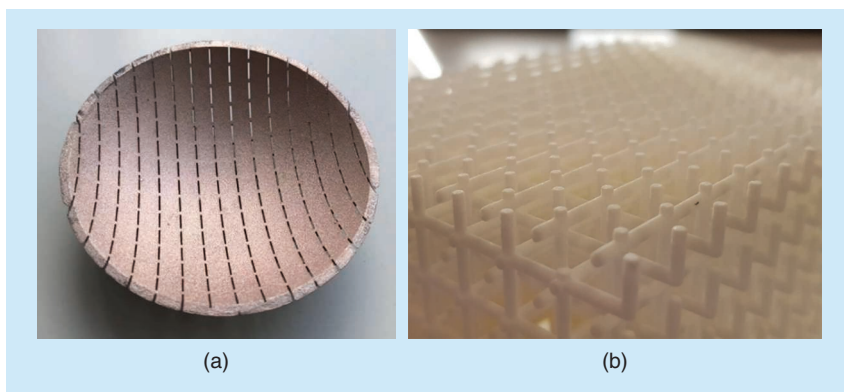


FIGURE 4. (a) A conductive coated conformal frequency-selective surface (FSS). The FSS was printed using stereolithography to achieve a lower surface roughness. (b) 3D-printed interlaced metamaterial meshes using SLS. For more information, see [15] and [30].

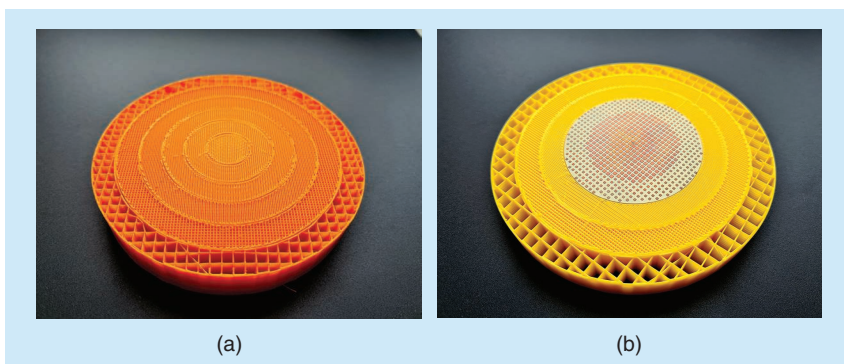


FIGURE 5. Two variations of a GRIN lens, where the dielectric properties are varied across the lens' radii. (a) A purely dielectric GRIN lens printed from ABS. (b) A GRIN lens printed from ABS with an added artificial dielectric disk providing an increased dielectric constant in the center. For more information, see [25] and [47].

Anisotropy has also been shown to create circular polarization when placed in the cavity of a Fabry–Pérot resonator antenna [51]. The 3D-printed metamaterial facilitated independent control of the axial ratio and directivity by controlling the phase difference in the standing waves of the two orthogonal electric field components inside the cavity. This paper also allowed the user to choose between linear polarization and circular polarization by mechanically rotating the metamaterial with respect to the antenna [51].

RAAs

RAAs are often popular in satellite applications, given their low-cost, low-profile, and high-gain characteristics. Typically, RAAs are constructed from circuit board substrates and consist of an array of metallic resonators backed by a ground plane. A horn is often used to feed the RA and is offset from the center so as to not interfere with the reflection. However, narrow bandwidths and ohmic/surface wave losses are associated with the metallic elements; to avoid this, dielectric resonators have been explored [52], [53], [54], [55]. With 3D printing, low-profile 3D RAAs can be realized.

The first reported FFF 3D-printed RA provided a high gain (20–28 dBi) over a wide bandwidth (26–34 GHz) [52]; see Figure 6(a). The 3D-printed structure contained 625 unit cells over the 12 × 12-cm surface. A phase response from 0 to 360° was achieved by varying the width of each dielectric element; therefore, the required phase distribution map can be converted into the CAD model to print. Similarly, unit cells with two orthogonal cuboids can also be used to convert a linearly polarized wave into a CP wave [53]; see Figure 6(b). By exploiting the extra degree of freedom, the width and height of both orthogonal cuboids were varied to change the orthogonal characteristics of the unit cells. This took extensive optimization via simulations and patient printing to create the delicate vertical architectures. Similar concepts have been used to generate four orbital angular momentum (OAM) modes at 30 GHz [54]. OAM is a growing research area, where multiple OAM modes can be carried in the same channel without interference, which can potentially increase channel capacity.

So far, the examples given all require a conductive ground plane to provide reflection, which suffers from ohmic losses.

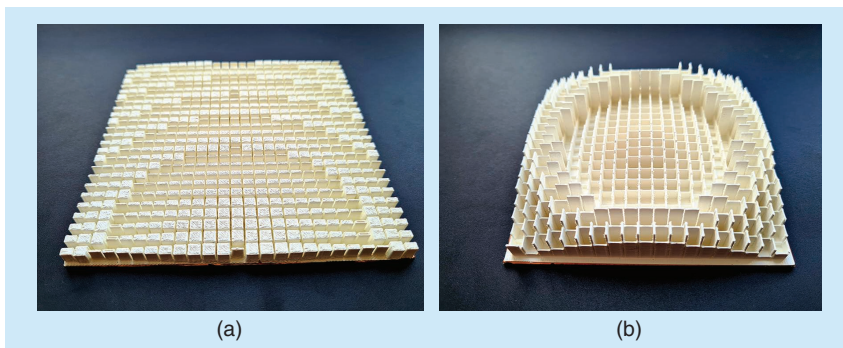


FIGURE 6. RAAs that were 3D printed from thermoplastic filaments, with (a) a thermoplastic ϵ_r value of 4.4, where the effective permittivity of each unit cell was varied by changing the inclusion width, and (b) a thermoplastic ϵ_r value of 7.4, where the effective permittivity of the unit cells was varied by changing the inclusion height. For more information, see [52] and [53].

Using a dielectric mirror, an all-dielectric RA was 3D printed [55]. Layers of dielectric slabs separated by air gaps were used to create a dielectric mirror with bandgaps in the V- and K-bands. As the frequency increases, the reflections at each interface interfere with one another and can cause total reflections. Outside the bandgap, the structure is transparent to EM waves. The PLA and air thicknesses were 1.5 and 3 mm at 18–27 GHz and 0.8 and 1 mm at 40–75 GHz. By using multiple layers, a dual-band device was 3D printed [55].

DIELECTRIC RESONATOR ANTENNAS

Dielectric resonator antennas (DRAs) typically require materials with relative permittivity values on the order of 10–20. With new developments in thermoplastic–ceramic composite filaments for RF applications, 3D printing DRAs is possible. The efficiency of DRAs is highly dependent on the loss tangents of the materials. DRAs typically have homogenous structures that are simple geometric shapes. This is partly due to limitations of conventional manufacturing techniques. 3D printing may not be the optimal manufacturing route for DRAs, but it can provide a quick fabrication route, with extra degrees of freedom in terms of the shape and including heterogenous properties. The bandwidth-versus-the-maximum-gain tradeoff has been analyzed via hundreds of simulations in [56].

3D printing was used to print a DRA that was composed of series of rings, with the highest ϵ_r at the center. The ϵ_r values were 10, 8.25, four, and 2.5 and were all 3D printed from one material by varying the local volume fraction of air. This design combined the transverse magnetic (TM) modes (TM_{01δ}, TM_{02δ}, and TM_{03δ}) to create a wide impedance bandwidth. Changing the 3D-printed infill fraction was also used to create a DRA with two effective dielectric regions. It was found that by increasing the air volume fraction in certain locations and including a metal cap to compensate for the frequency shift, the weight of the DRA could be reduced by 22% [57].

3D PRINTED CERAMIC COMPONENTS

3D printing ceramics involves expensive equipment (which includes the 3D printer and a furnace) and expert knowledge in materials. For these reasons, it is easier (and often quicker) to produce components with thermoplastics and resins. However, processing ceramics opens the possibility of higher-permittivity and lower-loss materials, higher temperature and power handling capabilities of the printed parts, and the potential for printing metal pastes.

A relatively easy method of manufacturing ceramic parts is the vat polymerization method with a preformulated ceramic-loaded resin. The resulting structure can then undergo rebinding and sintering to remove the resin and fuse the ceramic powder together.

Published examples include an LL manufactured from MgTiO_3 [58], an anisotropic CP DRA [59], and a dielectric CP helical antenna manufactured from zirconia [60].

Through process such as DIW, ceramics and metals can be printed together in the same component; however, this is a growing research area that faces considerable challenges of material compatibility and component warping due to unmatched thermal expansion coefficients. Current works demonstrate the potential of transmission lines and ring resonators printed on high-permittivity ceramics [13] in addition to miniaturized patch antennas by fully embedding the resonating patch in the ceramic [12]; an example is given in Figure 7.

METALIZED WAVEGUIDES AND HORN ANTENNAS

There have been many papers in recent years that have used 3D printing of dielectrics that are then electro- or electroless plated to form metal devices for RF applications. These are often waveguides and horn antennas, and the aim is to replicate the behavior of the fully metal version with a reduced manufacturing time and weight. The latter has particular relevance for the aviation and space industries [61]. There is a tradeoff in the optimal frequency of applications: at low frequencies, the metallization may not be thick enough to contain enough skin depths, whereas at higher frequencies, the surface roughness of the printed layers becomes a problem unless further postprocessing is implemented. The ease of manufacturing more complicated shapes allows the RF designer to imagine innovative designs that would be difficult with conventional subtractive techniques. Examples of these designs include a 3D helical antenna with nested tapered helices (2.4 and 5.4 GHz) [62], a cavity-backed slot antenna (4.8–7.5 GHz) [63], a coax-to-waveguide transition (8 GHz) [14], a 3D-printed Ku-band four-element steerable phased-array antenna with a fully integrated beam forming network [64], an ultrawideband Vivaldi antenna (10–15 GHz) taking advantage of its 3D shape to increase the bandwidth [65], a corrugated horn (11–13 GHz) [66], a K-band array antenna with waveguides that include water channels for cooling for high-power devices [67], a turnstile junction orthomode transducer for polarization separation in a waveguide (75–110 GHz) [68], and rectangular horn antennas, parabolic mirrors, and polarizers at 140–220 GHz [69].



FIGURE 7. A 3D-printed DIW metal-ceramic microstrip patch with silver and a high-permittivity, low-loss, and low-sintering-temperature ceramic ($\text{Ag}_2\text{Mo}_2\text{O}_7$). For more information, see [12].

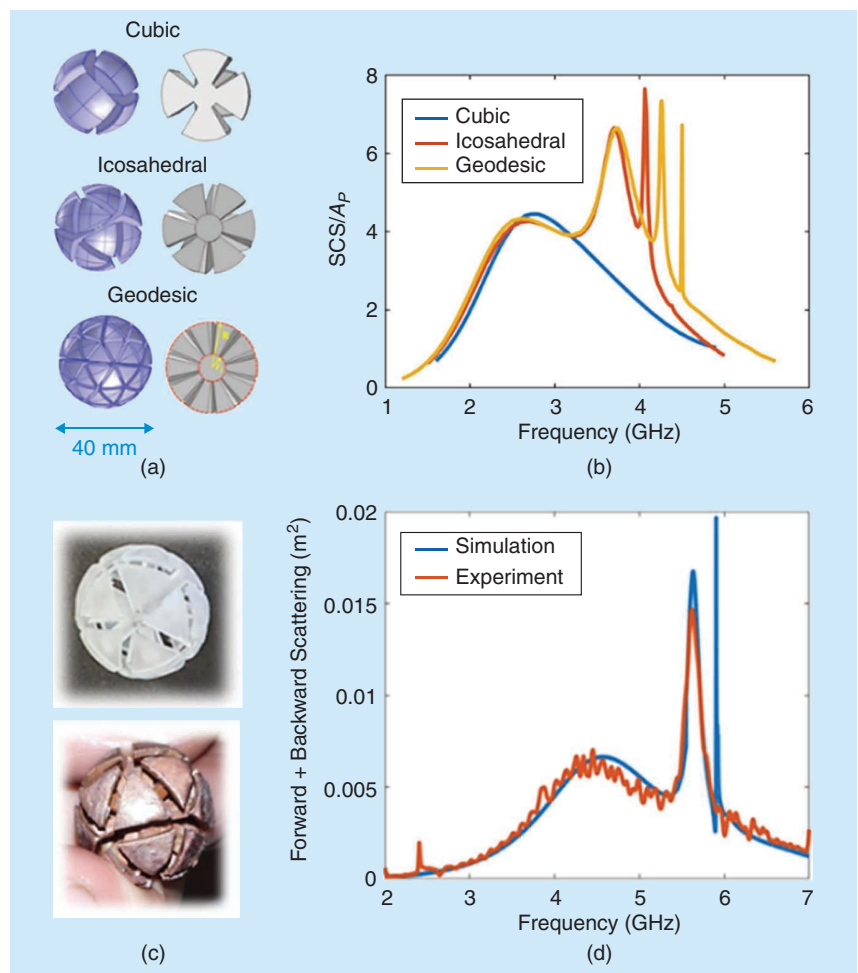


FIGURE 8. (a) The scattering cross section and electric near field of the first two modes of a metacube made from three crossed rods with square plates. (b) The scattering cross section and electric near field of the first two modes of a meta-icosahedron made from 10 crossed rods with triangular plates. (c) An experimental demonstration of scattering: the radar cross section of the particles measured in the forward and backward directions compared with simulations on Comsol. Inset: 3D-printed samples of icosahedra electroplated in copper (some plates have been removed to reveal the interior structure). (d) The simulated scattering cross section of the meta-icosahedron in (b) and an equivalently sized spherical particle made of a Drude metal, with a plasma frequency determined by the rod-and-plate structure.

METAPARTICLES FOR ISOTROPIC MULTIMODE MICROWAVE SCATTERING

Control over the scattering behavior of EM waves is key for applications from antenna design [70], [71] to energy harvesting [72] to radar detection [73]. Subwavelength scatterers are an attractive means to achieve this due to their powerful scattering of radiation at their resonance condition and their small physical size. Metallic nanoparticles create a powerful scattering effect at optical frequencies by coupling free electrons oscillations at the surface of the metal with the electric field of incident radiation, an effect known as a *surface plasmon*. However, this behavior depends on electric field penetration into the particle since at microwave frequencies, metals are near-perfect electrical conductors, the fields are almost perfectly screened, and the powerful scattering due to surface plasmons cannot be excited.

It has been shown that the texturing of a metal surface can lead to the excitation of surface waves that mimic this plasmon behavior (“spoof” plasmons) [74], [75], [76], but these effects have been mostly limited to 2D metasurfaces and extrusions of 2D shapes. 3D metaparticles that can convincingly mimic this behavior have proved difficult to realize, and previous works attempting to reproduce these effects have been limited in both the functionality of their design and the performance of fabricated samples, due to available manufacturing methods [73], [77], [78], [79].

3D printing has enabled the scalable fabrication of complex metaparticles that can fully reproduce the powerful scattering of plasmonic nanoparticles at microwave frequencies. Spheres with a textured outer layer with symmetries based on the platonic solids [depicted in Figure 8(a)] are shown to powerfully scatter EM radiation in a manner comparable to that of metal nanoparticles at optical frequencies. The number of modes the particle can support is determined by the patterning of the particle outer layer, as shown in Figure 8(b), enabling control over the scattering power, bandwidth, and directionality (as higher-order resonances scatter more powerfully in the forward direction) simply by choosing the number and dimensions of grooves in identical metal spheres. Spheres with patterning corresponding to the highest-order platonic solid (the icosahedron) were 3D printed through vat polymerization (stereolithography) and then metalized via electroplating; both unplated and copper-plated metaparticles are presented in Figure 8(c). These particles can be shown to support three modes, which correspond to the dipole, quadrupole, and octupole plasmonic resonances. Experimental measurements of the forward and backward scattering of these particles in an anechoic chamber show excellent agreement with the simulations, as in Figure 8(d), and have applications in superdirective antennas and control over radar scattering.

CONCLUSIONS

3D printing of microwave components is a fast-growing research topic, as additive manufacturing provides many versatile methods of manufacturing components. 3D printing is ideal for low–mid-scale production of high-value components when conventional manufacturing techniques are not suitable. FFF is the most accessible method of 3D printing, as the machines

are relevantly inexpensive and there is a wide range of easily accessible materials. Other methods, such as vat polymerization and PBF, are capable of much finer resolutions but are not capable of multimaterial printing. Ceramic and metal printing are achievable with PBF and ceramic/metal powders and with DIW and ceramic slurries/metal pastes. Naturally, printing with ceramics and metals will lead to parts with lower dielectric and conductive losses; however, the manufacturing complexity increases since these parts often need to be fired/sintered in a second process. Additional information and links can be found in the supplementary information available at <https://www.doi.org/10.1109/MAP.2022.3229298>.

ACKNOWLEDGMENT

This work was supported by Engineering and Physical Sciences Research Council grants “Synthesizing 3D Metamaterials for Radio-Frequency, Microwave, and Terahertz Applications” (EP/N010493/1) and “Anisotropic Microwave/Terahertz Metamaterials for Satellite Applications” (EP/S030301/1). This article has supplementary information, provided by the authors, available at <https://www.doi.org/10.1109/MAP.2022.3229298>.



AUTHOR INFORMATION

Thomas Whittaker (t.whittaker@lboro.ac.uk) is a research associate with the Wolfson School of Mechanical, Electrical, and Manufacturing Engineering, Loughborough University, Loughborough LE11 3TU U.K. His research interests include 3D-printed microwave components and circuits, material characterization, metasurfaces, satellite communications, and anisotropy.

Shiyu Zhang (s.zhang@lboro.ac.uk) is with the Wolfson School of Mechanical, Electrical, and Manufacturing Engineering, Loughborough University, Loughborough LE11 3TU U.K. His research interests include engineered metamaterials, metasurfaces, frequency-selective surfaces, antennas and radio-frequency circuit components, additive manufacturing, and wearable antennas.

Alexander Powell (a.w.powell@exeter.ac.uk) is a research fellow in the Department of Physics and Astronomy, University of Exeter, Exeter EX4 4PY U.K. His research interests include developing novel 3D scattering particles (metatoms), which have example use cases in superdirective antennas, lenses, and superscatterers.

Chris J. Stevens (chris.stevens@eng.ox.ac.uk) is a professor in the Department of Engineering Science, University of Oxford,

Oxford OX1 3PJ U.K. His research interests include ultrawide-band communications, metamaterials, ultrafast nanoelectronics, high-speed electromagnetics, and magnetic metamaterials.

John (Yiannis) C. Vardaxoglou (j.c.vardaxoglou@lboro.ac.uk) is a professor in the Wolfson School of Mechanical, Electrical, and Manufacturing Engineering, Loughborough University, Loughborough LE11 3TU U.K, where he established the Wireless Communications Research Group. He has been awarded 20 research grants and published more than 400 journal and conference papers. He is a Fellow of IEEE.

William Whittow (w.g.whittow@lboro.ac.uk) is a professor of radio-frequency materials at Loughborough University, Loughborough LE11 3TU U.K, where he leads the Wireless Communications Research Group. He has the principal investigator on £14 million of research grants and authored more than 280 journal and conference papers. He is a Senior Member of IEEE.

REFERENCES

- [1] D. Helena, A. Ramos, T. Varum, and J. N. Matos, "Antenna design using modern additive manufacturing technology: A review," *IEEE Access*, vol. 8, pp. 177,064–177,083, Sep. 2020, doi: 10.1109/ACCESS.2020.3027383.
- [2] C.-K. Lee et al., "Evaluation of microwave characterization methods for additively manufactured materials," *Designs*, vol. 3, no. 4, Sep. 2019, Art. no. 47, doi: 10.3390/designs3040047.
- [3] C. J. Stevens, I. Spanos, A. Vallechi, J. McGhee, and W. Whittow, "3D printing of functional metal and dielectric composite meta-atoms," *Small*, vol. 18, no. 10, pp. 1–9, Jan. 2022, doi: 10.1002/smll.202105368.
- [4] T. Goulas et al., "The impact of 3D printing process parameters on the dielectric properties of high permittivity composites," *Designs*, vol. 3, no. 4, Nov. 2019, Art. no. 50, doi: 10.3390/designs3040050.
- [5] P. S. Grant et al., "Manufacture of electrical and magnetic graded and anisotropic materials for novel manipulations of microwaves," *Philos. Trans. A*, vol. 373, no. 2049, Aug. 2015, Art. no. 20140353, doi: 10.1098/rsta.2014.0353.
- [6] F. Castles et al., "Microwave dielectric characterisation of 3D-printed BaTiO₃/ABS polymer composites," *Scientific Rep.*, vol. 6, no. 1, Mar. 2016, Art. no. 22714, doi: 10.1038/srep22714.
- [7] N. Duangrit et al., "Terahertz dielectric property characterization of photopolymers for additive manufacturing," *IEEE Access*, vol. 7, pp. 12,339–12,347, Jan. 2019, doi: 10.1109/ACCESS.2019.2893196.
- [8] W. Nawrot and K. Malecha, "Additive manufacturing revolution in ceramic microsystems," *Microelectron. Int.*, vol. 37, no. 2, pp. 79–85, May 2020, doi: 10.1108/MI-11-2019-0073.
- [9] J. C. Snyder and K. A. Thole, "Understanding laser powder bed fusion surface roughness," *J. Manuf. Sci. Eng.*, vol. 142, no. 7, Jul. 2020, Art. no. 071003, doi: 10.1115/1.4046504.
- [10] O. A. Peverini et al., "Selective laser melting manufacturing of microwave waveguide devices," *Proc. IEEE*, vol. 105, no. 4, pp. 620–631, Apr. 2017, doi: 10.1109/JPROC.2016.2620148.
- [11] A. Goulas et al., "Microstructure and microwave dielectric properties of 3D printed low loss Bi₂Mo₂O₉ ceramics for LTCC applications," *Appl. Mater. Today*, vol. 21, Dec. 2020, Art. no. 100862, doi: 10.1016/j.apmt.2020.100862.
- [12] A. Goulas et al., "Additively manufactured ultra-low sintering temperature, low loss Ag₂Mo₂O₇ ceramic substrates," *J. Eur. Ceram. Soc.*, vol. 41, no. 1, pp. 394–401, Jan. 2021, doi: 10.1016/j.jeurceramsoc.2020.08.031.
- [13] R. Gheisari et al., "Multi-material additive manufacturing of low sintering temperature Bi₂Mo₂O₉ ceramics with Ag floating electrodes by selective laser burnout," *Virtual Phys. Prototyping*, vol. 15, no. 11, pp. 1–15, Jan. 2020, doi: 10.1080/17452759.2019.1708026.
- [14] C. Guo et al., "A 3-D printed ϵ -plane waveguide magic-T using air-filled coax-to-waveguide transitions," *IEEE Trans. Microw. Theory Techn.*, vol. 67, no. 12, pp. 4984–4994, Dec. 2019, doi: 10.1109/TMTT.2019.2944355.
- [15] H. F. Álvarez et al., "3D conformal bandpass millimeter-wave frequency selective surface with improved fields of view," *Scientific Rep.*, vol. 11, no. 1, Dec. 2021, Art. no. 12846, doi: 10.1038/s41598-021-91218-y.
- [16] R. Colella, F. P. Chietera, F. Montagna, A. Greco, and L. Catarinucci, "Customizing 3D-printing for electromagnetics to design enhanced RFID antennas," *IEEE J. Radio Freq. Identif.*, vol. 4, no. 4, pp. 452–460, Dec. 2020, doi: 10.1109/jrfid.2020.3001043.
- [17] M. J. Kim et al., "One-step electrodeposition of copper on conductive 3D printed objects," *Additive Manuf.*, vol. 27, pp. 318–326, May 2019, doi: 10.1016/j.addma.2019.03.016.
- [18] F. Sun, Y. Li, L. Ge, and J. Wang, "Millimeter-wave magneto-electric dipole antenna array with a self-supporting geometry for time-saving metallic 3-D printing," *IEEE Trans. Antennas Propag.*, vol. 68, no. 12, pp. 7822–7832, Dec. 2020, doi: 10.1109/TAP.2020.3016158.
- [19] M. Ferrando-Rocher, J. I. Herranz-Herruzo, A. Valero-Nogueira, and B. Bernardo-Clemente, "Selective laser sintering manufacturing as a low cost alternative for flat-panel antennas in millimeter-wave bands," *IEEE Access*, vol. 9, pp. 45,721–45,729, Mar. 2021, doi: 10.1109/ACCESS.2021.3067637.
- [20] J. Cao, H. Wang, S. Tao, S. Mou, and Y. Guo, "Highly integrated beam scanning groove gap waveguide leaky wave antenna array," *IEEE Trans. Antennas Propag.*, vol. 69, no. 8, pp. 5112–5117, Aug. 2021, doi: 10.1109/TAP.2020.2995470.
- [21] J. Wu, C. Wang, and Y. Guo, "A wideband circularly polarized array antenna with compact and high-efficiency feeding network," *IEEE Trans. Antennas Propag.*, vol. 68, no. 1, pp. 62–69, Jan. 2020, doi: 10.1109/TAP.2019.2935093.
- [22] K. Johnson et al., "Digital manufacturing of pathologically-complex 3D printed antennas," *IEEE Access*, vol. 7, pp. 39,378–39,389, Mar. 2019, doi: 10.1109/ACCESS.2019.2906868.
- [23] L. Lewin, "The electrical constants of a material loaded with spherical particles," *Proc. Inst. Electr. Eng.*, vol. 94, no. 27, pp. 65–68, Jan. 1947, doi: 10.1049/ji-3-2.1947.0013.
- [24] S. Zhang, W. Whittow, and J. C. Vardaxoglou, "Additively manufactured artificial materials with metallic meta-atoms," *IET Microw., Antennas Propag.*, vol. 11, no. 14, pp. 1955–1961, Nov. 2017, doi: 10.1049/iet-map.2016.0952.
- [25] S. Zhang, R. K. Arya, W. G. Whittow, D. Cadman, R. Mittra, and J. C. Vardaxoglou, "Ultra-wideband flat metamaterial GRIN lenses assisted with additive manufacturing technique," *IEEE Trans. Antennas Propag.*, vol. 69, no. 7, pp. 3788–3799, July 2021, doi: 10.1109/TAP.2020.3044586.
- [26] Y. Rahmat-Samii, J. Budhu, R. E. Hodges, D. C. Hofmann, and D. Ruffatto, "A novel 60-cm nonspherical 3-D printed voxelized lens antenna: Design, fabrication and measurement," in *Proc. IEEE Int. Symp. Antennas Propag. USNC-URSI Radio Sci. Meeting*, Jul. 2019, pp. 1699–1700, doi: 10.1109/APUSNCURSINRSM.2019.8889115.
- [27] A. Massaccesi, P. Pirinoli, and J. C. Vardaxoglou, "A multilayer unit-cell for perforated dielectric transmitarray antennas," in *Proc. IEEE Int. Symp. Antennas Propag. USNC/URSI Nat. Radio Sci. Meeting*, 2019, pp. 263–264, doi: 10.1109/APUSNCURSINRSM.2018.8608712.
- [28] T. W. Whittaker, W. G. Whittow, and J. C. Vardaxoglou, "Artificially engineered capacitors for discrete high-frequency electronic circuitry," *IEEE Trans. Microw. Theory Techn.*, vol. 68, no. 1, pp. 74–86, Jan. 2020, doi: 10.1109/TMTT.2019.2950224.
- [29] A. Vallecchi, A. Radkovskaya, L. Li, G. Faulkner, C. J. Stevens, and E. Shamonina, "Superdirective dimers of coupled self-resonant split ring resonators: Analytical modelling and numerical and experimental validation," *Scientific Rep.*, vol. 10, no. 1, Dec. 2020, Art. no. 274, doi: 10.1038/s41598-019-56988-6.
- [30] A. W. Powell, R. C. Mitchell-Thomas, S. Zhang, D. A. Cadman, A. P. Hibbins, and J. R. Sambles, "Dark mode excitation in three-dimensional interlaced metallic meshes," *ACS Photon.*, vol. 8, no. 3, pp. 841–846, Mar. 2021, doi: 10.1021/acsp Photonics.0c01811.
- [31] T. Hayat, M. U. Afzal, A. Lalbakhsh, and K. P. Esselle, "3-D-printed phase-rectifying transparent superstrate for resonant-cavity antenna," *IEEE Antennas Wireless Propag. Lett.*, vol. 18, no. 7, pp. 1400–1404, Jul. 2019, doi: 10.1109/LAWP.2019.2917767.
- [32] A. Bisognin et al., "Ball grid array-module with integrated shaped lens for WiGig applications in eyewear devices," *IEEE Trans Antennas Propag.*, vol. 64, no. 3, pp. 872–882, Mar. 2016, doi: 10.1109/TAP.2016.2517667.
- [33] S. Ooms and P. Reynaert, "A 120-GHz wireless link using 3D-printed lens with flexible dielectric fiber feed and 28-nm CMOS transceiver," *IEEE Solid-State Circuits Lett.*, vol. 3, no. 1, pp. 142–145, Jul. 2020, doi: 10.1109/LSSC.2020.3008224.
- [34] J. Budhu and Y. Rahmat-Samii, "3D-printed inhomogeneous dielectric lens antenna diagnostics: A tool for assessing lenses misprinted due to fabrication tolerances," *IEEE Antenna Propag. Mag.*, vol. 62, no. 4, pp. 49–61, Aug. 2020, doi: 10.1109/MAP.2019.2946566.
- [35] K. V. Hoel, M. Ignatenko, S. Kristoffersen, E. Lier, and D. S. Filipovic, "3-D printed monolithic GRIN dielectric-loaded double-ridged horn antennas," *IEEE Trans. Antennas Propag.*, vol. 68, no. 1, pp. 533–539, Jan. 2020, doi: 10.1109/TAP.2019.2938563.
- [36] S. Zhang, D. Cadman, and J. C. Vardaxoglou, "Additively manufactured profiled conical horn antenna with dielectric loading," *IEEE Antennas Wireless Propag. Lett.*, vol. 17, no. 11, pp. 2128–2132, Nov. 2018, doi: 10.1109/LAWP.2018.2871029.
- [37] S. Rashid et al., "3-D printed UWB microwave bodyscope for biomedical measurements," *IEEE Antennas Wireless Propag. Lett.*, vol. 18, no. 4, pp. 626–630, Apr. 2019, doi: 10.1109/LAWP.2019.2899591.

- [38] S. Sarjoghian, Y. Alfadhl, X. Chen, and C. G. Parini, "A 3-D-printed high-dielectric materials-filled pyramidal double-ridged horn antenna for abdominal fat measurement system," *IEEE Trans. Antennas Propag.*, vol. 69, no. 1, pp. 64–73, Jan. 2021, doi: 10.1109/TAP.2020.3008653.
- [39] S. Sarjoghian, M. H. Sagor, Y. Alfadhl, and X. Chen, "A 3D-printed high-dielectric filled elliptical double-ridged horn antenna for biomedical monitoring applications," *IEEE Access*, vol. 7, pp. 94,977–94,985, Jul. 2019, doi: 10.1109/ACCESS.2019.2928629.
- [40] S. Zhang, P. Liu, and W. Whittow, "Design and fabrication of 3-D-printed high-gain broadband Fresnel zone lens using hybrid groove-perforation method for millimeter-wave applications," *IEEE Antennas Wireless Propag. Lett.*, vol. 21, no. 1, pp. 34–38, Jan. 2022, doi: 10.1109/LAWP.2021.3116459.
- [41] B. Vial, T. Whittaker, S. Zhang, W. G. Whittow, and Y. Hao, "Optimization and experimental validation of a bi-focal lens in the microwave domain," *AIP Adv.*, vol. 12, no. 2, Feb. 2022, Art. no. 025103, doi: 10.1063/5.0074062.
- [42] C. Mu, S. Fang, H. Liu, Z. Wang, and S. Fu, "3-D-printed dielectric lens with cone-shaped cavity for axial ratio beamwidth enhancement of circularly polarized patch antenna," *IEEE Access*, vol. 7, pp. 105,062–105,071, Jul. 2019, doi: 10.1109/ACCESS.2019.2931938.
- [43] Y. Li, L. Ge, M. Chen, Z. Zhang, Z. Li, and J. Wang, "Multibeam 3-D-printed Luneburg lens fed by magnetolectric dipole antennas for millimeter-wave MIMO applications," *IEEE Trans. Antennas Propag.*, vol. 67, no. 5, pp. 2923–2933, May 2019, doi: 10.1109/TAP.2019.2899013.
- [44] C. Wang, Y. Xia, G. Guo, M. Nasir, and Q. Zhu, "Ellipsoidal Luneburg lens binary array for wide-angle scanning," *IEEE Trans. Antennas Propag.*, vol. 68, no. 7, pp. 5702–5707, Jul. 2020, doi: 10.1109/TAP.2020.2969875.
- [45] C. Wang, J. Wu, and Y.-X. Guo, "A 3-D-printed wideband circularly polarized parallel-plate Luneburg lens antenna," *IEEE Trans. Antennas Propag.*, vol. 68, no. 6, pp. 4944–4949, Jun. 2020, doi: 10.1109/TAP.2019.2955222.
- [46] K. Liu, C. Zhao, S. W. Qu, Y. Chen, J. Hu, and S. Yang, "A 3-D-printed multi-beam spherical lens antenna with ultrawide-angle coverage," *IEEE Antennas Wireless Propag. Lett.*, vol. 20, no. 3, pp. 411–415, Mar. 2021, doi: 10.1109/LAWP.2021.3054042.
- [47] S. Zhang, R. K. Arya, S. Pandey, Y. Vardaxoglou, W. Whittow, and R. Mittra, "3D-printed planar graded index lenses," *IET Microw., Antennas Propag.*, vol. 10, no. 13, pp. 1411–1419, Oct. 2016, doi: 10.1049/iet-map.2016.0013.
- [48] Q.-Y. Guo, Q. W. Lin, and H. Wong, "A high gain millimeter-wave circularly polarized Fabry-Pérot antenna using PRS-integrated polarizer," *IEEE Trans. Antennas Propag.*, vol. 69, no. 2, pp. 1179–1183, Feb. 2021, doi: 10.1109/TAP.2020.3011110.
- [49] G.-B. Wu, Y.-S. Zeng, K. F. Chan, S.-W. Qu, and C. H. Chan, "3-D printed circularly-polarized lens antenna operating at terahertz frequencies," in *Proc. URSI Int. Symp. Electromagn. Theory (EMTS)*, 2019, vol. 67, no. 7, pp. 4429–4437, doi: 10.23919/URSI-EMTS.2019.8931543.
- [50] J. Zhu et al., "3-D printed planar dielectric linear-to-circular polarization conversion and beam-shaping lenses using coding polarizer," *IEEE Trans. Antennas Propag.*, vol. 68, no. 6, pp. 4332–4343, Jun. 2020, doi: 10.1109/TAP.2020.2972625.
- [51] F. Wu and K. M. Luk, "Circular polarization and reconfigurability of Fabry-Pérot resonator antenna through metamaterial-loaded cavity," *IEEE Trans. Antennas Propag.*, vol. 67, no. 4, pp. 2196–2208, Apr. 2019, doi: 10.1109/TAP.2019.2893213.
- [52] S. Zhang, "Three-dimensional printed millimetre wave dielectric resonator reflectarray," *IET Microw., Antennas Propag.*, vol. 11, no. 14, pp. 2005–2009, Nov. 2017, doi: 10.1049/iet-map.2017.0278.
- [53] Q. Cheng et al., "Dual circularly polarized 3-D printed broadband dielectric reflectarray with a linearly polarized feed," *IEEE Trans. Antennas Propag.*, vol. 70, no. 7, pp. 5393–5403, Jul. 2022, doi: 10.1109/TAP.2022.3142735.
- [54] B. Li, P. F. Jing, L. Q. Sun, K. W. Leung, and X. Lv, "3D printed OAM reflectarray using half-wavelength rectangular dielectric element," *IEEE Access*, vol. 8, pp. 142,892–142,899, Aug. 2020, doi: 10.1109/ACCESS.2020.3013678.
- [55] J. Zhu, Y. Yang, D. McGloin, S. Liao, and Q. Xue, "3-D printed all-dielectric dual-band broadband reflectarray with a large frequency ratio," *IEEE Trans. Antennas Propag.*, vol. 69, no. 10, pp. 7035–7040, Oct. 2021, doi: 10.1109/TAP.2021.3076528.
- [56] E. B. Whiting, S. D. Campbell, G. Mackertich-Sengerdy, and D. H. Werner, "Dielectric resonator antenna geometry-dependent performance tradeoffs," *IEEE Open J. Antennas Propag.*, vol. 2, pp. 14–21, 2021, doi: 10.1109/ojap.2020.3037826.
- [57] M. Cuevas, F. Pizarro, A. Leiva, G. Hermosilla, and D. Yunge, "Parametric study of a fully 3D-printed dielectric resonator antenna loaded with a metallic cap," *IEEE Access*, vol. 9, pp. 73,771–73,779, May 2021, doi: 10.1109/ACCESS.2021.3081068.
- [58] Y.-H. Lou, Y.-X. Zhu, G.-F. Fan, W. Lei, W.-Z. Lu, and X.-C. Wang, "Design of Ku-band flat Luneburg lens using ceramic 3-D printing," *IEEE Antennas Wireless Propag. Lett.*, vol. 20, no. 2, pp. 234–238, Feb. 2021, doi: 10.1109/LAWP.2020.3046489.
- [59] C. D. Morales, C. Morlaas, A. Chabory, R. Pascaud, M. Grzeskowiak, and G. Mazingue, "3D-printed ceramics with engineered anisotropy for dielectric resonator antenna applications," *Electron. Lett.*, vol. 57, no. 18, pp. 679–681, Aug. 2021, doi: 10.1049/ell2.12234.
- [60] S. Wang et al., "Radar cross-section reduction of helical antenna by replacing metal with 3-D printed zirconia ceramic," *IEEE Antennas Wireless Propag. Lett.*, vol. 19, no. 2, pp. 350–354, Feb. 2020, doi: 10.1109/LAWP.2019.2962524.
- [61] K. Glatre, L. Hildebrand, E. Charbonneau, J. Perrin, and E. Amyotte, "Paving the way for higher-volume cost-effective space antennas: Designing for manufacturing, assembly, integration, and test," *IEEE Antennas Propag. Mag.*, vol. 61, no. 5, pp. 47–53, Oct. 2019, doi: 10.1109/MAP.2019.2932313.
- [62] Y. Tawk, "A dynamic dual tapered 3-D printed nested helical antenna," *IEEE Trans. Antennas Propag.*, vol. 68, no. 2, pp. 697–702, Feb. 2020, doi: 10.1109/TAP.2019.2943427.
- [63] M. Amjadi and K. Sarabandi, "Ultra-wideband, compact, and high-gain two-port antenna system for full-duplex applications," *IEEE Trans. Antennas Propag.*, vol. 69, no. 11, pp. 7173–7182, Nov. 2021, doi: 10.1109/TAP.2021.3076266.
- [64] S. Shin et al., "Polymer-based 3-D printed Ku-band steerable phased-array antenna subsystem," *IEEE Access*, vol. 7, pp. 10,6662–10,6673, Aug. 2019, doi: 10.1109/ACCESS.2019.2932431.
- [65] V. Gjokaj, J. Papapolymerou, J. D. Albrecht, B. Wright, and P. Chahal, "A compact receive module in 3-D printed Vivaldi antenna," *IEEE Trans. Compon., Packag. Manuf. Technol.*, vol. 10, no. 2, pp. 343–346, Feb. 2020, doi: 10.1109/TCPMT.2019.2961345.
- [66] L. Wu, H. Chu, D. Cao, S. Peng, and Y. Guo, "3-D printed antenna subsystem with dual-polarization and its test in system level for radiometer applications," *IEEE Access*, vol. 8, pp. 127,856–127,865, Jul. 2020, doi: 10.1109/ACCESS.2020.3008727.
- [67] B. Zhang et al., "A metallic 3-D printed airborne high-power handling magneto-electric dipole array with cooling channels," *IEEE Trans. Antennas Propag.*, vol. 67, no. 12, pp. 7368–7378, Dec. 2019, doi: 10.1109/TAP.2019.2935085.
- [68] J. Shen and D. S. Ricketts, "Compact W-band 'Swan Neck' turnstile junction orthomode transducer implemented by 3-D printing," *IEEE Trans. Microw. Theory Techn.*, vol. 68, no. 8, pp. 3408–3417, Aug. 2020, doi: 10.1109/TMTT.2020.2992065.
- [69] S.-H. Shin, X. Shang, N. M. Ridler, and S. Lucyszyn, "Polymer-based 3-D printed 140–220 GHz low-cost quasi-optical components and integrated subsystem assembly," *IEEE Access*, vol. 9, pp. 28,020–28,038, Feb. 2021, doi: 10.1109/ACCESS.2021.3057606.
- [70] A. E. Krasnok, C. R. Simovski, P. A. Belov, and Y. S. Kivshar, "Superdirective dielectric nanoantennas," *Nanoscale*, vol. 6, no. 13, pp. 7354–7361, Jul. 2014, doi: 10.1039/c4nr01231c.
- [71] A. E. Krasnok, A. E. Miroshnichenko, P. A. Belov, and Y. S. Kivshar, "Huygens optical elements and Yagi-Uda nanoantennas based on dielectric nanoparticles," *JETP Lett.*, vol. 94, no. 8, pp. 593–598, Dec. 2011, doi: 10.1134/S0021364011200070.
- [72] Y. Zhai et al., "Scalable-manufactured randomized glass-polymer hybrid metamaterial for daytime radiative cooling," *Science*, vol. 355, no. 6329, pp. 1062–1066, Mar. 2017, doi: 10.1126/science.aai7899.
- [73] A. W. Powell et al., "Strong, omnidirectional radar backscatter from sub-wavelength, 3D printed metacubes," *IET Microw., Antennas Propag.*, vol. 14, no. 14, pp. 1862–1868, Nov. 2020, doi: 10.1049/iet-map.2020.0178.
- [74] J. B. Pendry, L. Martín-Moreno, and F. J. García-Vidal, "Mimicking surface plasmons with structured surfaces," *Science*, vol. 305, no. 5685, pp. 847–848, Aug. 2004, doi: 10.1126/science.1098999.
- [75] M. J. Lockyear, A. P. Hibbins, and J. R. Sambles, "Microwave surface-plasmon-like modes on thin metamaterials," *Phys. Rev. Lett.*, vol. 102, no. 7, Feb. 2009, Art. no. 073901, doi: 10.1103/PhysRevLett.102.073901.
- [76] A. Pors, E. Moreno, L. Martín-Moreno, J. B. Pendry, and F. J. García-Vidal, "Localized spoof plasmons arise while texturing closed surfaces," *Phys. Rev. Lett.*, vol. 108, no. 22, May 2012, Art. no. 223905, doi: 10.1103/PhysRevLett.108.223905.
- [77] D. Muha, M. Mlakar, S. Hrbar, and D. Zaluski, "Practical realization of isotropic RF replica of plasmonic sphere," in *Proc. 6th Eur. Conf. Antennas Propag. (EuCAP)*, 2012, pp. 2706–2709, doi: 10.1109/EUCAP.2012.6206495.
- [78] D. Muha, M. Mlakar, S. Hrbar, D. Zaluski, and M. Martinis, "Analysis of magnetic response of circular arrangement of RF replicas of isotropic plasmonic spheres," in *Proc. 20th Int. Conf. Appl. Electromagn. Commun.*, 2010, pp. 1–4.
- [79] S. Hrbar, Z. Eres, and H. Kumric, "Spherical resonators acting as RF replicas of plasmonic nanospheres," in *Proc. IEEE Antennas Propag. Soc. AP-S Int. Symp.*, 2007, pp. 4340–4343, doi: 10.1109/APS.2007.4396502.